17

The Effect of Variable Na/K on the CO_2 Content of Slab-Derived Rhyolitic Melts

Michelle Muth[1,2], Megan S. Duncan[3], and Rajdeep Dasgupta[1]

ABSTRACT

We conducted high pressure, high temperature experiments to investigate the effect of variable alkali ratio on the CO_2-rich fluid solubility in hydrous rhyolitic melts at sub-arc depths. Experiments were performed at 3.0 and 1.5 GPa, 1300 °C on rhyolitic compositions similar to low-degree partial melts of subducted slab lithologies, with fixed total alkalis (Na_2O+K_2O ~11.5 wt.%, volatile-free), but Na# (molar $Na_2O/[Na_2O+K_2O]$) varying from 0.15 to 0.88. In the experimental glasses, total dissolved CO_2 ($CO_2^{tot.}$) ranged from 2.14 ± 0.07 to 3.20 ± 0.07 wt.% at 3.0 GPa, and from 0.70 ± 0.02 to 1.19 ± 0.02 wt.% at 1.5 GPa. Experiments showed a general positive correlation between Na# and $CO_2^{tot.}$, with the exception of the highest Na# experiment at 1.5 GPa. Carbon was dissolved as molecular CO_2 ($CO_2^{mol.}$) and carbonate (CO_3^{2-}). As Na# increased, $CO_2^{mol.}/CO_2^{tot.}$ decreased from 0.94 to ~0.00 in the 1.5 GPa experiments and from 0.65 to 0.05 in the 3.0 GPa experiments. Variability in CO_2 concentration is larger and more clearly correlated with Na# at 3.0 GPa, indicating that this effect is pressure dependent. Our results show that compositional variability in silicic melts must be considered to accurately place constraints on the limit of CO_2 transfer in subduction zones.

17.1. INTRODUCTION

On million-year to billion-year timescales, the whole Earth carbon cycle is controlled by exchange between two reservoirs: the exosphere, which includes the atmosphere, crust, and ocean, and the mantle. This exchange plays an important role in long-term climate variability and in deep earth dynamics (Dasgupta & Hirschmann, 2010; Hayes & Waldbauer, 2006; Sleep & Zahnle, 2001). While the outgassing of carbon occurs through magmatic and volcanic processes at many volcanic centers, ingassing is achieved via subducting slabs that contain carbonated basaltic crust and carbon-bearing sediments (Dasgupta, 2013; Dasgupta & Hirschmann, 2010; Kelemen & Manning, 2015). As these slabs pass beneath volcanic arcs, a portion of this slab carbon is transported upward into the volcanic arc mantle source. The remaining carbon is transported to greater depths, where it may eventually be released into other areas of the mantle (e.g., Thomson et al., 2016) or become effectively sequestered within the residual slab material. The proportion of carbon released from the slab at sub-arc conditions and the exact agent that transports carbon to the arc magma mantle source remains incompletely constrained.

Measurements of carbon isotopes and $CO_2/^3He$ ratios of volcanic arcs indicate that ~71%–96% of carbon outgassed comes from the subducted slab (de Leeuw et al., 2007; Sano & Williams, 1996; Shaw et al., 2003). Most subduction zones today are likely too cold to liberate significant amounts of stored carbon via dry partial melting or decarbonation. However, increasing evidence indicates that many subduction zones likely undergo

[1] *Department of Earth, Environmental and Planetary Sciences, Rice University, Houston, Texas, USA*

[2] *Department of Earth Sciences, University of Oregon, Eugene, Oregon, USA*

[3] *Department of Geosciences, Virginia Tech, Blacksburg, Virginia, USA*

Carbon in Earth's Interior, Geophysical Monograph 249, First Edition. Edited by Craig E. Manning, Jung-Fu Lin, and Wendy L. Mao.

fluid-saturated slab melting (e.g., Kerrick & Connolly, 2001), and that this melt is a feasible carrier of CO_2 into arc source regions (Cooper et al., 2012; Duncan & Dasgupta, 2015; Martin & Hermann, 2018; Skora et al., 2015; Syracuse et al., 2010). Therefore, carbon carrying capacity, as CO_2, of the slab partial melt places an upper limit on the amount of carbon that reaches arc source regions from subducting slabs. Previous work that considered melting of subducted lithologies found that with the exception of carbonatitic and carbonated silicate melts generated at comparatively high pressures (e.g., Thomsen & Schmidt, 2008; Tsuno et al., 2012), the partial melts generated were generally rhyolitic in composition (Figure 17.1; e.g. Schmidt, 2015). Therefore, determining CO_2 carrying capacity of rhyolitic partial melts is crucial to understanding carbon flux in subduction settings.

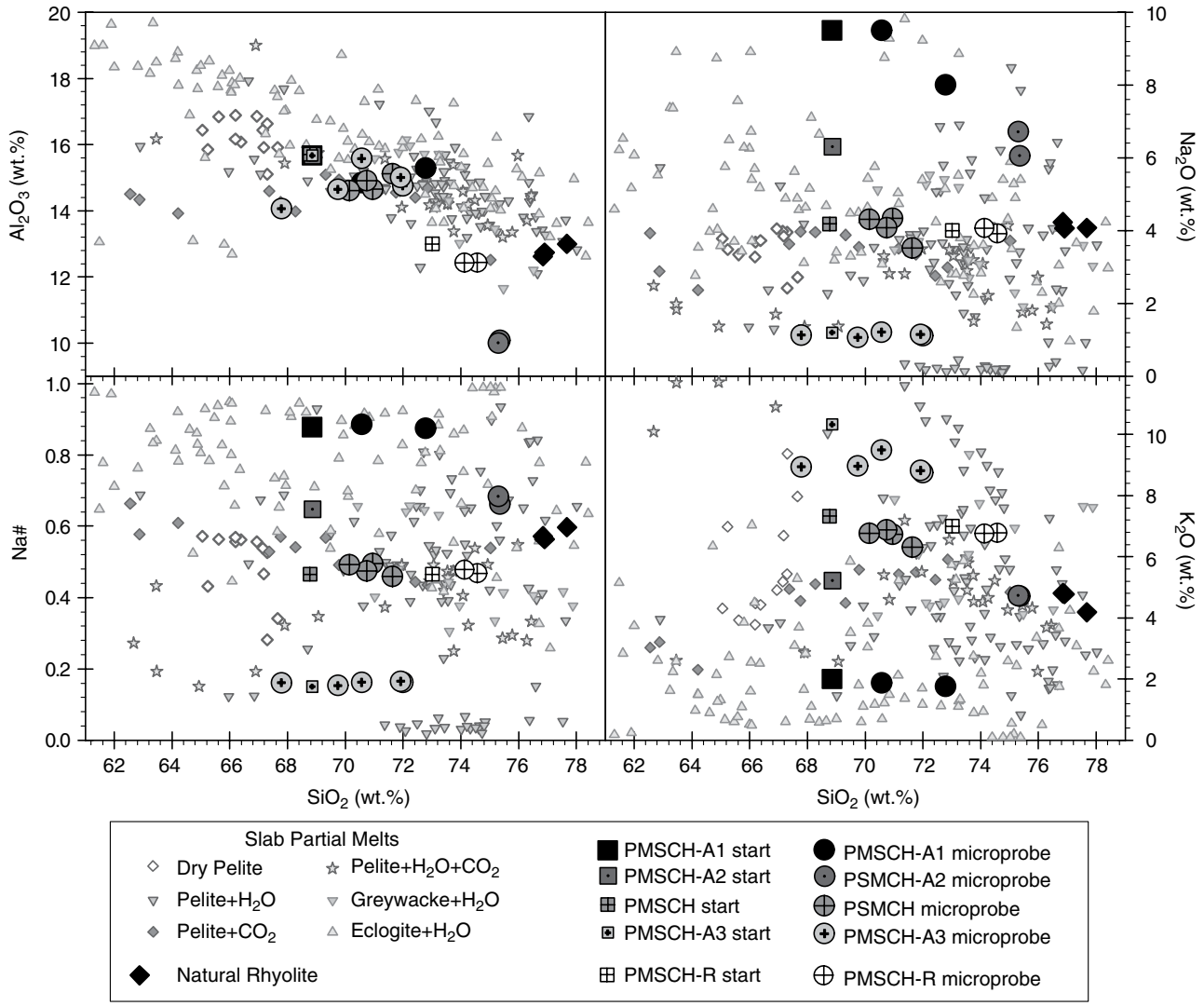

Figure 17.1 Starting compositions (squares) and microprobe analysis (circles) of volatile-free starting compositions (Table 17.1), compared with past experimental work on CO_2 dissolution in hydrous rhyolite (PMSCH; Duncan & Dasgupta, 2014), past experimental work that determined partial melt compositions of slab lithologies: dry metapelite (open diamonds; Spandler et al., 2010); fluid-present, hydrous pelite (inverted triangles; Hermann & Green, 2001; Hermann & Spandler, 2008; Johnson & Plank, 1999; Schmidt et al., 2004; Tsuno & Dasgupta, 2012); dry, carbonated pelite (gray diamonds; Tsuno & Dasgupta, 2011); fluid-present, hydrous, carbonated pelite (stars; Thomsen & Schmidt, 2008; Tsuno & Dasgupta, 2012); hydrous graywacke (inverted triangles; Auzanneau et al., 2006; Schmidt et al., 2004); hydrous basalt (triangles; Carter et al., 2015; Klimm et al., 2008; Laurie & Stevens, 2012; Mann & Schmidt, 2015; Martin & Hermann, 2018; Prouteau et al., 2001; Qian & Hermann, 2013; Rapp & Watson, 1995; Sen & Dunn, 1994; Skora et al., 2015; Wolff et al., 2013); and natural rhyolite compositions from previous CO_2 solubility studies (large black diamonds; Blank et al., 1993; Fogel & Rutherford, 1990; Tamic et al., 2001). See electronic version for color representation of the figures in this book.

Many previous studies that investigated the CO_2 solubility of rhyolitic melts were either at pressure-temperature (*P-T*) conditions not relevant to the sub-arc mantle (Blank et al., 1993; Fogel & Rutherford, 1990; Tamic et al., 2001), or used simplified melt compositions (Brey, 1976; Mysen, 1976; Mysen et al., 1976; Mysen & Virgo, 1980a). More recent work (Duncan & Dasgupta, 2014, 2015) investigated the CO_2 carrying capacity of slab-derived melts by focusing on CO_2 dissolution in a model rhyolitic partial melt composition of subducted slab lithologies over the appropriate *P-T* range. These studies found that differences in CO_2 dissolution in silicate melts were linked to the degree of melt polymerization caused by varying amounts of SiO_2 or H_2O (Fogel & Rutherford, 1990; Mysen, 1976), where less polymerized melts have a higher CO_2 capacity (e.g., Brooker et al., 2001; Eguchi & Dasgupta, 2018).

Other factors controlling melt polymerization include major cation proportions, which are a potentially important control on CO_2 capacity. Dixon (1997) presented a model that incorporates a CO_2 dependence on relative amounts of Ca^{2+}, Mg^{2+}, Na^{+}, and K^{+} in basaltic melts, consistent with subsequent studies that found CO_2 concentrations in mafic melts increased with total alkali content (e.g. Ni & Keppler, 2013) and that for mafic-ultramafic melts both Ca^{2+} and Mg^{2+} complexes with CO_3^{2-}, with the affinity of Ca^{2+} being much stronger (Duncan et al., 2017). One study at low pressures found that melt CO_2 capacity increased with increasing Na# = $Na_2O/(Na_2O+K_2O)$ on a molar basis, in phonotephritic melts (Vetere et al., 2014), while another found the opposite trend in nephelinitic melts (Morizet et al., 2014). This contradiction may be due to other differing compositional factors between the two studies. No similar work has been done in rhyolitic partial melts, and the contradictory results of the two previous studies, albeit on more silica-poor melts, leaves a gap in our knowledge on the possible effect of Na# on CO_2 carrying capacity of slab-derived silicic melts. Given that rhyolitic melts are poor in Ca, Mg, and Fe, Na# is an important compositional variable to explore.

In combination with a wide range of *P-T* conditions, compositional heterogeneity in subducting materials produce a wide spectrum of partial melt compositions. Previous experiments that determined partial melt compositions of both silicic sediment and hydrous basalt report a wide range of Na# from 0.07 to 0.98 (Figure 17.1, see caption for references). This ratio is sensitive to the *P-T* conditions at which a melt is generated; Na becomes more compatible in residual lithologies at high pressures, driving a decrease in Na# in partial melts with increasing pressure (Poli & Schmidt, 2002).

To investigate the compositional dependence of CO_2 dissolution in slab-derived, hydrous, silicic melts, we conducted piston cylinder experiments on rhyolitic partial melts under *P-T* conditions relevant to subduction zones. In order to isolate the effects of alkalis from other cations, we focused our investigation on compositions with variable alkali ratios that were otherwise identical.

17.2. METHODS

17.2.1. Starting Material

Starting compositions were variations of the PMSCH composition from Duncan and Dasgupta (2014), which in turn was modeled from previous studies of low-degree partial melts of subducted lithologies (Figure 17.1, Table 17.1). The three main starting compositions for this study were identical to PMSCH in all major elements except for Na_2O and K_2O, which varied in concentration while maintaining a fixed total alkali content (~11.5 wt.%). Na# ranged from 0.15 to 0.88, which spans the Na# of both sediment and hydrous basalt partial melts. Synthetic starting compositions were made from powders of oxides (SiO_2, TiO_2, Al_2O_3, MnO_2, MgO, P_2O_5) and carbonates ($FeCO_3$, $CaCO_3$, Na_2CO_3, K_2CO_3) to add ~7 wt.% CO_2, and $Al(OH)_3$ to add ~3 wt.% H_2O (Table 17.1). To further assess the effects of H_2O and SiO_2 on CO_2 dissolution, two additional mixes were made: one with a Na# of 0.15 but a higher H_2O content, and a second with a Na# of 0.46 but a slightly higher concentration of SiO_2 (PMSCH-R). In the subsequent discussions, we focus primarily on experimental results from the three main compositions. Starting oxides were fired for several hours prior to mixing to avoid excess absorbed water. Components were then weighed, mixed, and ground in ethanol for 60 minutes to homogenize the starting powder, then stored in a 110 °C oven along with assembly parts to minimize moisture absorption.

17.2.2. Experimental Technique

Experiments were conducted in an end-loaded piston cylinder device in a half-inch $BaCO_3$ assembly at Rice University. $Au_{75}Pd_{25}$ capsules containing the starting mixtures were embedded in crushable MgO spacers. Pressure calibration and temperature gradient for this assembly and apparatus is reported in Tsuno and Dasgupta (2011). Temperature was controlled and monitored using a type C thermocouple, placed above the capsule, separated by a 1 mm MgO disc. Experiments were pressurized to 3.0 GPa or 1.5 GPa, then heated at 100 °C/min to 1300 °C and held for 48 hours, after which they were quenched by turning off power to the heater while maintaining pressure on the assembly. The capsule was then depressurized slowly, cut in half with a wire saw, set in PETROPOXY 154, and polished for analysis.

Table 17.1 Starting compositions used in the experiments.

Comp.	PMSCH-A1	PMSCH-A2	PMSCH-A3[a]	PMSCH-R	PMSCH[b]
SiO_2	68.85	68.87	68.86	73.01	68.77
TiO_2	0.50	0.50	0.50	0.30	0.50
Al_2O_3	15.68	15.67	15.67	13.00	15.71
FeO	0.99	0.99	0.99	0.88	0.99
MnO	0.50	0.50	0.50	0.34	0.50
MgO	0.09	0.09	0.09	0.26	0.19
CaO	1.47	1.47	1.47	1.00	1.47
Na_2O	9.51	6.30	1.20	4.00	4.19
K_2O	2.01	5.22	10.33	7.00	7.33
P_2O_5	0.41	0.38	0.39	0.21	0.35
Total	100.00	100.00	100.00	100.00	100.00
Na#	0.88	0.65	0.15	0.46	0.46
NBO/T	0.10	0.08	0.04	0.07	0.06
H_2O	8.46	7.83	6.80	6.95	7.49
$CO_2^{tot.}$	3.00	3.00	3.00	3.00	3.00

[a] This mix was made twice; the second contained a water content ~8 wt.%.
[b] Compositions re-reported from Duncan and Dasgupta (2014).

17.2.3. Analytical Techniques

Major elements were measured using a Cameca SX 100 electron microprobe at NASA Johnson Space Center, with an accelerating voltage of 15 kV, an electron beam current of 10 nA, and a 20 μm spot. Counting times for Si, Al, Ca, Ti, Fe, Mn, and Mg were 30 s on peak and 10 s on each background, and for Na, P, and K were 20 s on peak and 10 s on each background. Natural minerals and synthetic glasses were used as analytical standards. Averages of analyses on several spots of each experiment on each glass are reported in Table 17.2.

CO_2 and H_2O speciation and abundances were determined using a Thermo Nicolet Fourier Transform Infrared Spectrometer at Rice University. Experimental glasses were doubly polished to 15–50 μm, then cleaned with acetone before analysis. Conditions were set to 128 scans, at 4 cm^{-1} resolution, and a 40 μm spot size under a nitrogen purge. Peaks attributed to water were detected at 3530 cm^{-1} (OH^-+H_2O: O-H stretching) and at 1630 cm^{-1} (molecular water). Peaks attributed to carbon were detected at 2349 cm^{-1} (molecular CO_2, $CO_2^{mol.}$) and from 1425 cm^{-1} to 1530 cm^{-1} (carbonate doublet, CO_3^{2-}); concentration of CO_3^{2-}, calculated as CO_2, was determined using the 1425 cm^{-1} peak, and total dissolved CO_2 ($CO_2^{tot.}$) was simply $CO_2^{mol.} + CO_3^{2-}$. Peak heights and areas were measured with linear backgrounds.

Volatile concentrations in the glass were quantified with the Beer-Lambert law:

$$C_i = 100 * M_i A_j / d \rho \varepsilon_j, \quad (17.1)$$

where C_i is the concentration of species i in weight percent, M_i is the molecular weight of the species, A_j is the absorbance of band j, unitless or in cm^{-1}, d is the thickness of the section in cm, ρ is the calculated density of the glass in g L^{-1} (Lange & Carmichael, 1987; Silver, 1988), and ε_j is the absorption coefficient for the peak j in L mol^{-1} cm^{-1} or L mol^{-1} cm^{-2} from previous studies (Duncan & Dasgupta, 2015; Silver & Stolper, 1989; Stolper et al., 1987). Sample thickness was measured using a digital micrometer after the analysis and calculated using the "interference fringe" method (Tamic et al., 2001) that uses $\lambda = 1/2dn$ with an empirical value for refractive index (n) and λ measured from each spectrum.

17.3. RESULTS

17.3.1. Texture and Major Element Composition

Quench products showed a glassy phase with large, rounded vesicles, indicating the presence of a CO_2-rich vapor phase. In each experimental glass, the electron microprobe total was less than 100%, ranging from 92.55% to 99.02%, suggesting the presence of dissolved volatiles (Table 17.2). While measured glass compositions generally match starting materials, at both pressures there were some deviations from the starting compositions. For example, experimental glasses from the three main compositions varied in SiO_2 content from ~68 to 75 wt.% and CaO content from ~1.2 to 1.6 wt.%. However, the measured analyses of a given composition were consistent.

We did attempt to estimate oxygen fugacity (fO_2) of these experiments based on the amount of iron that was dissolved in the AuPd capsule; unfortunately, the dissolved Fe concentrations were within the error of the measurement, making calculation of fO_2 highly uncertain. However, the absence of graphite in the quench products and evidence for equilibrium with a CO_2 rich

Table 17.2 Measured experimental glass compositions and run conditions.

	PMSCH-A1		PMSCH-A2		PMSCH-A3		PMSCH-A3[a]			PMSCH-R		PMSCH[b]	
Run No.	B311	B319	B316	B321	B331	B337	B308	B323	B322	B229	B231	B116	B139
P (GPa)	3.0	1.5	3.0	1.5	3.0	1.5	3.0	3.0	1.5	3.0	2.5	3.0	1.5
T (°C)	1300	1300	1300	1300	1300	1300	1300	1300	1300	1300	1300	1300	1300
T_{ae} (°C)	530	566	525	533	523	537	503	501	526	513	529	537	563
n	10	10	10	10	10	10	10	10	10	20	20	9	10
SiO_2	70.6 (1)	72.8 (3)	75.4 (8)	75.3 (2)	69.7 (2)	67.8 (3)	70.6 (4)	72.0 (3)	71.9 (2)	74.6 (3)	74.1 (4)	71.6 (3)	70.1 (2)
TiO_2	0.46 (3)	0.45 (2)	0.55 (4)	0.56 (5)	0.50 (3)	0.49 (4)	0.52 (3)	0.59 (2)	0.53 (3)	0.31 (3)	0.32 (3)	0.50 (3)	0.50 (2)
Al_2O_3	14.9 (1)	15.3 (2)	10.1 (2)	10.01 (6)	14.6 (2)	14.1 (1)	15.6 (2)	14.8 (2)	15.0 (1)	12.4 (2)	12.4 (3)	15.1 (1)	14.6 (2)
FeO	0.20 (4)	0.05 (3)	0.24 (8)	0.13 (3)	0.09 (5)	0.24 (4)	0.16 (3)	0.20 (5)	0.08 (2)	0.25 (7)	0.4 (1)	0.56 (9)	0.17 (4)
MnO	0.35 (3)	0.11 (2)	0.30 (5)	0.30 (5)	0.19 (5)	0.32 (5)	0.33 (5)	0.39 (4)	0.19 (3)	0.18 (5)	0.21 (4)	0.34 (4)	0.21 (3)
MgO	0.50 (5)	0.29 (3)	1.2 (4)	0.45 (3)	0.31 (2)	0.31 (3)	0.30 (2)	0.42 (3)	0.5 (1)	0.44 (3)	0.47 (4)	0.41 (1)	0.9 (2)
CaO	1.58 (6)	1.20 (4)	1.4 (3)	1.66 (5)	1.44 (5)	1.4 (1)	1.59 (6)	1.56 (8)	1.57 (5)	0.95 (7)	1.08 (6)	1.53 (5)	2.3 (2)
Na_2O	9.5 (1)	8.00 (9)	6.1 (2)	6.7 (1)	1.07 (5)	1.13 (7)	1.21 (6)	1.12 (5)	1.15 (4)	3.9 (2)	4.1 (1)	3.5 (1)	4.31 (8)
K_2O	1.87 (1)	1.76 (9)	4.7 (1)	4.7 (1)	9.0 (1)	8.9 (1)	9.49 (9)	8.75 (9)	8.8 (1)	6.8 (1)	6.8 (1)	6.3 (2)	6.77 (9)
P_2O_5	0.11 (5)	0.06 (6)	0.13 (6)	0.13 (8)	0.3 (1)	0.3 (1)	0.26 (8)	0.23 (1)	0.19 (5)	0.16 (8)	0.1 (1)	0.10 (7)	0.13 (7)
Total	97.62	99.02	95.13	97.03	97.23	95.07	92.55	93.49	96.94	92.96	92.88	97.52	96.35
Na#	0.89 (1)	0.87 (1)	0.66 (1)	0.68 (1)	0.15 (1)	0.16 (1)	0.16 (1)	0.16 (1)	0.17 (1)	0.47 (1)	0.48 (1)	0.459 (9)	0.492 (5)
NBO/T	0.104 (5)	0.038 (3)	0.15 (3)	0.149 (4)	0.011 (5)	0.027 (4)	0.016 (3)	0.019 (3)	0.015 (4)	0.065 (1)	0.075 (8)	0.035 (9)	0.1 (0)
H_2O[c]	2.84 (5)	1.67 (3)	3.18 (8)	2.6 (1)	3.01 (4)	2.3 (1)	4.91 (6)	5.27 (1)	2.88 (7)	3.86 (5)	2.81 (5)	2.45 (5)	1.70 (2)
$CO_2^{tot.d}$	3.20 (7)	0.70 (2)	3.10 (9)	1.19 (2)	2.14 (7)	0.81 (9)	2.01 (6)	2.02 (7)	0.77 (7)	1.80 (7)	1.84 (8)	1.95 (2)	0.82 (5)
$CO_2^{mol.}$	0.26 (2)	0.406 (1)	0.15 (2)	n.d.	1.40 (6)	0.76 (8)	1.44 (6)	1.42 (6)	0.68 (7)	0.61 (9)	0.65 (6)	1.00 (3)	0.11 (1)
CO_3^{2-}	2.94 (8)	0.30 (2)	2.9 (1)	1.18 (2)	0.74 (5)	0.05 (2)	0.58 (3)	0.60 (2)	0.099 (7)	1.2 (1)	1.19 (5)	0.95 (2)	0.71 (5)
$CO_2^{mol.}/CO_2^{tot.}$	0.081 (5)	0.58 (2)	0.048 (7)	n.a.	0.65 (2)	0.94 (2)	0.71 (1)	0.704 (9)	0.87 (1)	0.34 (5)	0.35 (2)	0.513 (1)	0.13 (1)
$CO_2^{mol.e}$	2.6 (2)	0.59 (5)	2.4 (2)	0.92 (8)	1.8 (1)	0.7 (1)	1.7 (1)	1.7 (1)	0.65 (9)	1.5 (1)	1.5 (1)	1.63 (9)	0.66 (8)
CO_3^{2-e}	0.6 (2)	0.12 (4)	0.7 (2)	0.26 (7)	0.3 (1)	0.13 (5)	0.3 (1)	0.3 (1)	0.12 (5)	0.3 (1)	0.3 (1)	0.32 (9)	0.16 (5)
$CO_2^{mol.}/CO_2^{tot.e}$	0.80 (5)	0.84 (5)	0.78 (6)	0.78 (6)	0.85 (4)	0.84 (4)	0.85 (4)	0.84 (4)	0.85 (4)	0.82 (5)	0.82 (5)	0.84 (5)	0.81 (5)

Note. Oxide concentrations are reported on a volatile-free basis with the 1σ error, in last digits cited, are given in parentheses based on spot to spot variation in EPMA and FTIR analyses for each sample; for example, 70.6 (1) wt.% should be read as 70.6 ± 0.1 wt.%. n = number of EMPA spots averaged.

[a] Exactly the same in all oxides as PMSCH-A3, but with a starting water content of ~8 wt.%.

[b] Compositions re-reported from Duncan and Dasgupta (2014).

[c] Water concentrations were calculated using absorption coefficients from Stolper et al. (1987) and Silver and Stolper (1989).

[d] Carbon concentrations were calculated using absorption coefficients from Duncan and Dasgupta (2015).

[e] Species concentrations recalculated using Konschak and Keppler (2014).

vapor phase indicates fO_2 conditions above the CCO (C + O_2 = CO_2) buffer.

17.3.2. Dissolved CO_2 and H_2O

Peak heights and shapes associated with $CO_2^{mol.}$ and CO_3^{2-} shifted with changing pressure and between each composition (Figure 17.2 a, b). At 3.0 GPa, with increasing Na#, the carbon species was increasingly dominated by CO_3^{2-}. The carbonate doublet also changed shape, with the doublet split decreasing with increasing Na#; in the high Na# glass, CO_3^{2-} peaks were asymmetrical and closely spaced at ~1504 cm^{-1} and 1439 cm^{-1}, while low Na# glass peaks were symmetrical and located at ~1530 cm^{-1} and ~1425 cm^{-1}. Experiments conducted at 1.5 GPa showed a similar, if less clearly delineated, trend. Unlike experiments at 3.0 GPa, the carbonate doublet did not show a progression in split or relative height, and became harder to detect, as it sits on the shoulder of Al-Si network peaks (~1600 and 1800 cm^{-1}; Newman et al., 1986) at the lowest Na#. The high Na# (Na# = 0.88) experiment at 1.5 GPa in particular had a carbonate doublet that looks distinctly different from its counterpart at 3.0 GPa.

Quantitative estimation of dissolved CO_2 and H_2O (Table 17.2) was performed from the collected FTIR spectra using previously determined absorption coefficients (Duncan & Dasgupta, 2015). In the main series of experiments, total dissolved CO_2 ranged from 2.14 ± 0.07 to 3.20 ± 0.07 wt.% at 3.0 GPa, and from 0.70 ± 0.02 to 1.19 ± 0.02 wt.% at 1.5 GPa (Figure 17.3d), with a general trend of increasing total CO_2 content with increasing Na#. The ratio of $CO_2^{mol.}/CO_2^{tot.}$ ranged from ~0.00 to 0.94 at 1.5 GPa to 0.05 to 0.65 at 3.0 GPa. Within both 1.5 GPa and 3.0 GPa experiments, there was a general

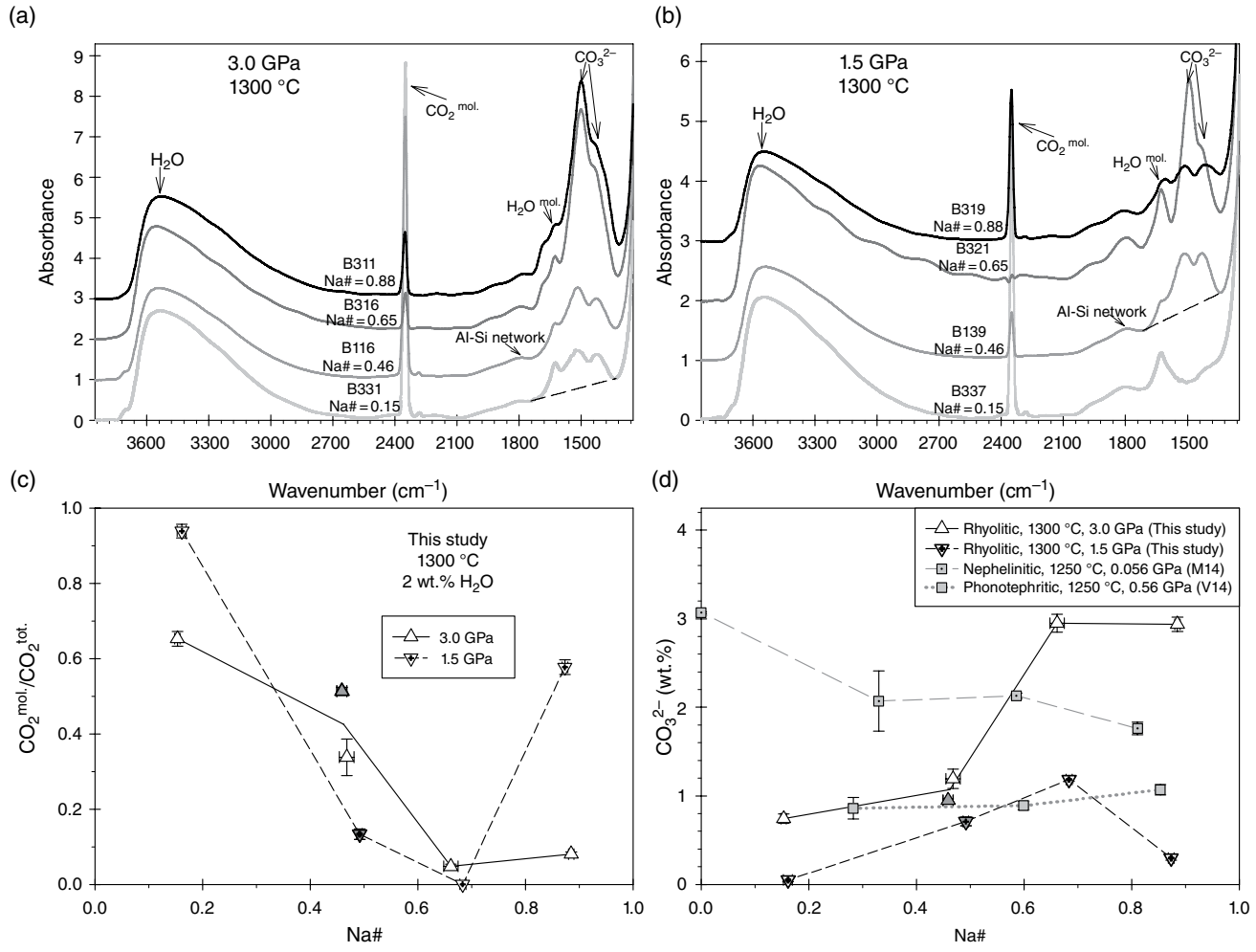

Figure 17.2 Top: FTIR spectra for each composition at (a) 3.0 GPa and (b) 1.5 GPa, marked with identified peak locations and Na# of each composition; gray Na# = 0.46 data are from Duncan and Dasgupta (2014). Bottom: Calculated (c) $CO_2^{mol.}/CO_2^{tot.}$ and (d) CO_3^{2-} estimated from the FTIR spectra, plotted versus Na#. Data shown for experiments at 1.5 GPa and 3.0 GPa. Data from previous studies on phonotephritic and nephelinitic compositions shown for comparison (squares; Morizet et al., 2014; Vetere et al., 2014). See electronic version for color representation of the figures in this book.

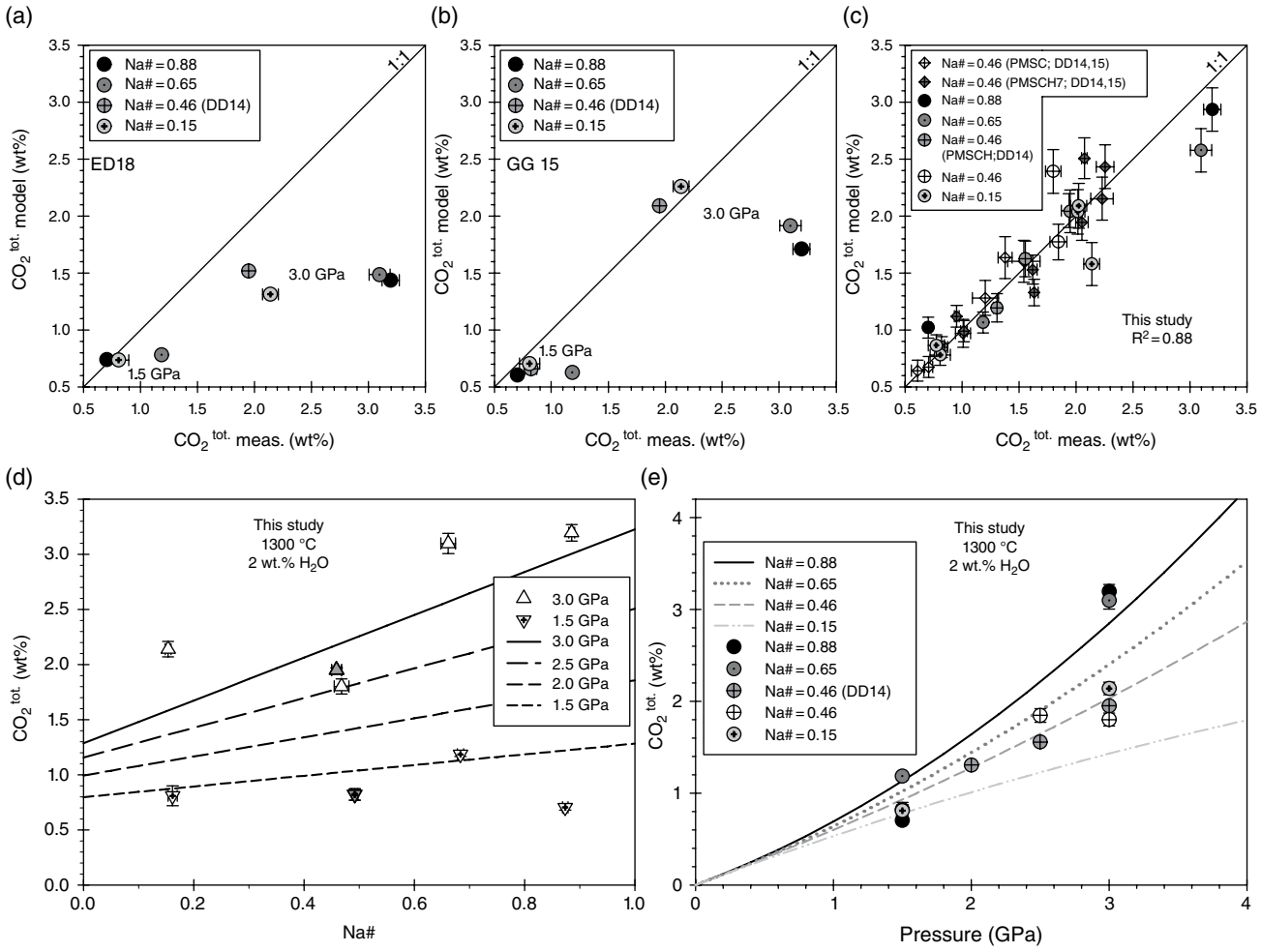

Figure 17.3 Measured CO_2 contents of rhyolitic glasses in this study compared to (a) the model of Eguchi and Dasgupta (2018), (b) the model of Ghiorso and Gualda (2015), and (c) values from our parameterization to show goodness of fit. All experimental data used for fitting are shown; see text for references. Calculated CO_2 content as a function of (d) Na#, as in Figure 17.4, and (e) pressure using equation (17.5) and an assumed H_2O content of 2 wt.%, with experimental data from the current study shown for comparison. Symbols as in Figure 17.1; DD14 = Duncan and Dasgupta (2014); DD15 = Duncan and Dasgupta (2015). See electronic version for color representation of the figures in this book.

trend of decreasing $CO_2^{mol.}$ with increasing Na#, while the behavior of CO_3^{2-} was the inverse, increasing with increasing Na# (Figure 17.2 c, d). At 3.0 GPa, experiments with slightly higher SiO_2 than the main series, composition PMSCH-R, contained 1.80 ± 0.07 wt.% total dissolved CO_2 with a $CO_2^{mol.}/CO_2^{tot.}$ value of 0.34. These values are comparable to results from experiments with the same Na#, compositions PMSCH, and are consistent with the observed patterns in CO_2 dissolution within the main series of experiments. An exception to this general behavior was the highest Na# experiment at 1.5 GPa, which had a lower CO_3^{2-} and $CO_2^{tot.}$ content than expected based on these overall trends.

It should be noted that the measured carbon speciation in the experimental glasses as determined using FTIR is likely affected during rapid cooling of the melts and that the actual magmatic speciation was different (see complete discussion in Duncan & Dasgupta, 2014). The measurement therefore represents the speciation at the glass transition temperature or apparent equilibrium temperature (T_{ae}, Table 17.2) that can be calculated for our experiments based on the dissolved water content (Zhang et al., 1995). Previous work showed that decreasing temperature toward T_{ae} will transform $CO_2^{mol.}$ to CO_3^{2-} (Morizet et al., 2001; Nowak et al., 2003), without changing the total amount of CO_2 dissolved. This effect was quantified, under limited experimental conditions (silicate melt compositions and water contents), by Konschak and Keppler (2014), who approximated the effect as:

$$\ln K = X_{CO_3^{2-}} / X_{CO_2^{mol.}} = \left[-2.69 - 21.38\left(\mathrm{NBO/T}\right)\right] + \left[1480 + 38810\left(\mathrm{NBO/T}\right)\right]/T \quad (17.2)$$

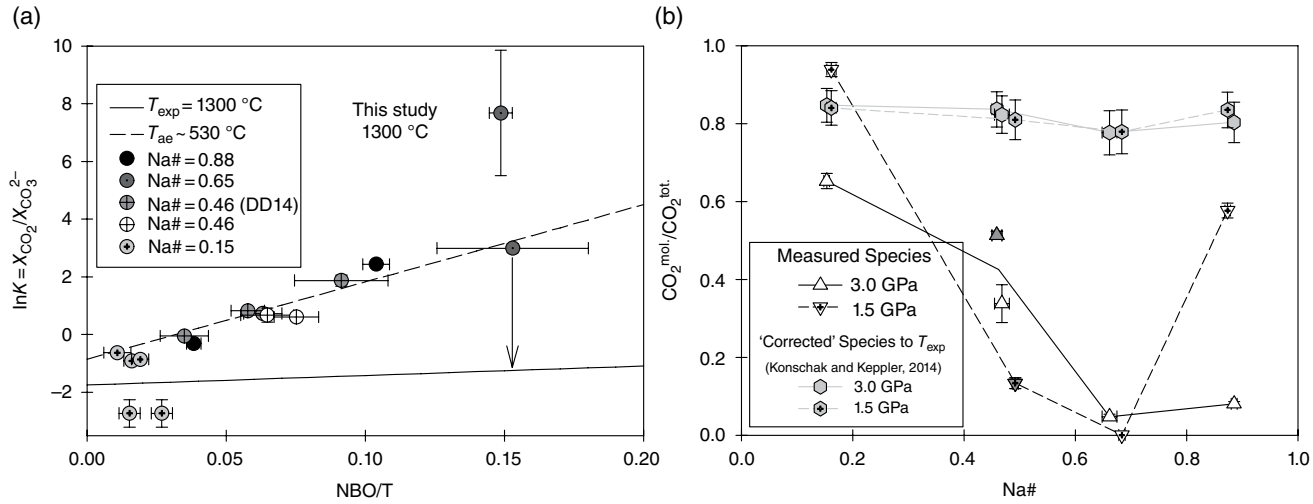

Figure 17.4 (a) Calculated ln*K* after Konschak and Keppler (2014) for experiments in this work and from Duncan and Dasgupta (2014) plotted as a function of estimated NBO/T. Various curves show the temperature dependence of ln*K* on silicate melt composition according to Konschak and Keppler (2014). Solid line: calculated ln*K* for our experimental temperatures (T_{exp}); dashed line: ln*K* determined for the apparent equilibrium temperatures (T_{ae}) calculated from Zhang et al. (1995). (b) Open triangles: $CO_2^{mol.}/CO_2^{tot.}$ values measured using FTIR on quenched glasses for experiments in this study and those from Duncan and Dasgupta (2014; DD14). Filled hexagons: "Corrected" $CO_2^{mol.}/CO_2^{tot.}$ values for the same experiments after Konschak and Keppler (2014). See electronic version for color representation of the figures in this book.

where NBO/T is a silicate compositional parameter (the ratio of nonbridging oxygens to tetrahedrally coordinated cations) and *T* is the temperature in K. When we "correct" our measured speciation from the T_{ae} to the experimental temperatures, all $CO_2^{mol.}/CO_2^{tot.}$ values are between 0.8 and 0.9 (Figure 17.4, Table 17.2). Given that NBO/T parameter does not account for differences in Na and K, only the total nonbridging oxygens, which is constant in our experiments, it is not surprising that "correcting" the data removes any trends in speciation as a function of Na#. Given the differences in CO_3^{2-} concentrations at different pressures and/or Na# but similar T_{ae}, we argue that the effect of pressure on enhanced CO_3^{2-} dissolution is real, although the absolute values of CO_2 solubility in the form of CO_3^{2-} may be influenced by quenching.

17.4. DISCUSSION

17.4.1. Composition-Dependent CO_2 Dissolution in Silicate Melt: Comparison to Previous Studies

Analysis of the experimental glasses showed that carbon was dissolved as $CO_2^{mol.}$ and CO_3^{2-} (Table 17.2). This suggests that the following carbon dissolution reactions were taking place (Mysen & Virgo, 1980b; Stolper et al., 1987):

$$\underset{\text{vapor}}{CO_2} \leftrightarrow \underset{\text{melt}}{CO_2} \tag{17.3}$$

$$\underset{\text{vapor}}{CO_2} + \underset{\text{melt}}{O^{2-}} \leftrightarrow \underset{\text{melt}}{CO_3^{2-}} \tag{17.4}$$

The previously discussed changes in carbonate doublet splitting visible in the FTIR spectra were likely caused by changes in the bonding environment of the carbonate group (e.g. Ni & Keppler, 2013). This observation combined with the positive correlation between the amount of CO_3^{2-} and Na# (Figure 17.2 c, d) suggests that at these conditions Na^+ may act as a stronger network modifier and therefore create melt carbonate complexes more effectively than K^+. Because of this, CO_3^{2-} may be accommodated more readily into the melt structure as Na# increases, explaining the simultaneous increase in CO_3^{2-} and total dissolved CO_2.

Variables besides Na# such as *P*, *T*, melt polymerization, and other cation concentrations also play a role in CO_2 dissolution and may moderate the effect of Na#. These compositional variables may explain the opposite trends seen in previous experiments (Morizet et al., 2014; Vetere et al., 2014), and variation within the general trends in the present study. For example, our high Na# experiment at 1.5 GPa, which contained less $CO_2^{tot.}$ and CO_3^{2-} than expected, contained approximately 0.4 wt.% less CaO than other compositions, which may have contributed to its anomalous behavior. However, $CO_2^{tot.}$ and CO_3^{2-} contents of experiments with a slightly more silicic composition, PMSCH-R, were consistent with the previously discussed patterns in Na#, $CO_2^{tot.}$, and $CO_2^{mol.}/CO_2^{tot.}$. This similarity suggests that small variations in

melt polymerization alone are not enough to generate the observed variations in CO_2 dissolution within our experiments.

Correlations in total CO_2 and $CO_2^{mol.}/CO_2^{tot.}$ were much stronger at 3.0 GPa than at 1.5 GPa (Figures 17.2 c, d, and 17.3d), indicating that the Na# effect is sensitive to pressure. Additionally, the observed range in total CO_2 dissolution and speciation was also larger in the 3.0 GPa experiments. Within the main experimental series at 1.5 GPa, the total dissolved CO_2 varied by 0.49 wt.% and $CO_2^{mol.}/CO_2^{tot.}$ varied by 0.60. In contrast, at 3.0 GPa the total dissolved CO_2 varied by 1.06 wt.% and $CO_2^{mol.}/CO_2^{tot.}$ varied by 0.94. This is consistent with CO_3^{2-} dissolution in silicic melt becoming important at higher pressures (Duncan & Dasgupta, 2014, 2015, 2017), where at higher pressure CO_2 behavior would be more sensitive to parameters such as Na# that influence dissolution of C in the melt as CO_3^{2-}.

The observed trend of increasing CO_3^{2-} with Na# in rhyolitic compositions (Figure 17.2d) is similar to the trend observed in a previous study conducted on phonotephritic composition (Vetere et al., 2014), and in contrast with the trend observed for a nephelinitic composition (Morizet et al., 2014). However, our experiments differ from this previous work in that we observed complex speciation (i.e., variable proportions of $CO_2^{mol.}$ and CO_3^{2-} within experimental glasses at the same pressure). As both of these previous studies were conducted at lower pressures on silica-poor compositions, it is difficult to make a direct comparison between their data and the current study.

Our data trends can also be compared with recent composition-dependent CO_2 solubility models for silicate melts (Figure 17.3 a, b; e.g. Eguchi & Dasgupta, 2018; Ghiorso & Gualda, 2015). While the model of Ghiorso and Gualda (2015) captures our low to intermediate CO_2 concentrations reasonably well, it does not capture the trend of increasing CO_2 with increasing Na# and as a consequence distinctly underpredicts our high CO_2 data. Because our CO_2 solubility data are for hydrous silicate melts, they cannot be compared directly with the model of Eguchi and Dasgupta (2018), which was built for nominally anhydrous systems and is expected to mostly underpredict CO_2 contents for melts with ~1–3 wt.% H_2O, where our data are focused. However, the model of Eguchi and Dasgupta (2018) also does not capture the specific trend of increasing $CO_2^{tot.}$ with increasing Na#, even when this difference in melt H_2O content is taken into account.

17.4.2. Parameterization

Because existing models that are applicable for a wide range of silicate melt compositions do not specifically capture the Na# effect observed in our study, we used all of the data from the current study and data from previous studies on natural rhyolitic compositions at high pressure (i.e. Duncan & Dasgupta, 2014, 2015) to derive an empirical fit of total dissolved CO_2 as a function of Na#. The variation in CO_2 speciation observed in our study and the opposing Na# effects observed in previous work (Morizet et al., 2014; Vetere et al., 2014) indicate that this effect is complex and is likely moderated by other compositional variables in addition to pressure and temperature. A comprehensive model describing the effect of Na# across a broad range of *P-T* conditions and major element compositions would require an expanded data set or intensive statistical treatment of available experimental data, both of which are beyond the scope of the current study. We focus here instead on creating an empirical parameterization to describe CO_2 solubility in natural rhyolitic melts at high pressure conditions.

The data set used in the empirical fit is drawn from a total of 31 experiments on rhyolitic compositions with variable Na#. Within these experiments, pressures range from 1.5 to 3.0 GPa, temperatures range from 1150 °C to 1300 °C, initial water contents range from 0 to ~8 wt.%, and Na# ranges from 0.15 to 0.89. This data was fit to a predefined form of equation using least-squares regression. This form of equation is similar to one used in previous work (Duncan & Dasgupta, 2014), where it was demonstrated that the effect of pressure is best described as a polynomial function. The other equation terms (Na#, X_{H2O}, T) describe the other variables within the data set and are arranged to provide the best fit to the data based on tests of several equation forms. This form of equation also captures the diminishing solubility of CO_2 as pressure approaches 1 atm. The equation and empirical fit are as follows:

$$\underset{\text{melt}}{CO_2}\left(\text{wt.\%}\right) = \left(a_1 \text{Na\#} + a_2 X_{H_2O} + a_3\right) P^2 + \left(b_1 T + b_2 X_{H_2O} + b_3\right) P \quad (17.5)$$

where X_{H2O} is mole fraction of H_2O in the melt, T is temperature in °C, and P is pressure in GPa. The constants are as follows: $a_1 = 2.16 \pm 0.04 \times 10^{-1}$, $a_2 = -4.07 \pm 0.07 \times 10^{-1}$, $a_3 = -2.8 \pm 0.1 \times 10^{-1}$, $b_1 = -5.6 \pm 0.4 \times 10^{-4}$, $b_2 = 3.7 \pm 0.1 \times 10^{0}$, $b_3 = 9.9 \pm 0.3 \times 10^{-1}$, $R^2 = 0.88$ (Figure 17.3c). The fit accounts for $CO_2^{mol.}$ and CO_3^{2-} as $CO_2^{tot.}$, but as this simple parameterization does not take into account the relative concentrations of the different dissolved species, it should not be used for melt compositions that are likely to have only CO_3^{2-} (such as basalts) or only $CO_2^{mol.}$ (such as rhyolites at low pressures). However, using $CO_2^{tot.}$ does remove any potential effects of quench-modified speciation. It can be applied to rhyolitic melts at pressures, temperatures, and H_2O, SiO_2, and CaO contents close to the calibration data set as detailed above.

Comparisons of modeled and predicted values show that this empirical fit does a reasonable job of capturing CO_2 dissolution within the calibration data set (Figure 17.3c). Based on the relative difference between the modeled and predicted values, experiments within the main series that deviate most from our fit are the low Na# experiment at 3.0 GPa (~35% difference), the high Na# experiment at 1.5 GPa (~31% difference), and the intermediate Na# (Na# = 0.66) experiment at 3.0 GPa (~20% difference). This is expected, as these experiments differ from overall trends within the data set (Figures 17.2 and 17.3). In order to compare the behavior of this parameterization to experimental data, we fixed temperature (1300 °C) and water content (~2 wt.%) and calculated CO_2 as a function of Na# (Figure 17.3d) and pressure (Figure 17.3e). Calculated CO_2 contents spread farther apart between each composition with increasing pressure. This is consistent with our data, which as previously discussed indicate that pressure has an effect on the importance of Na# in CO_2 dissolution.

Although the simple empirical parameterization describes our data overall, there are other compositional factors that influenced the measured CO_2 concentrations. For example, despite our attempt to hold all other oxide compositions constant, the experimental glasses varied in SiO_2 and CaO content. Given the widely recognized roles of melt polymerization and melt CaO on CO_2 dissolution, these variations might have contributed towards the variation of measured total CO_2. However, these compositional variations are smaller than the Na# variation, and therefore, our Na#-based parameterization captures most of the dissolved CO_2 variability observed in our experiments, to first order.

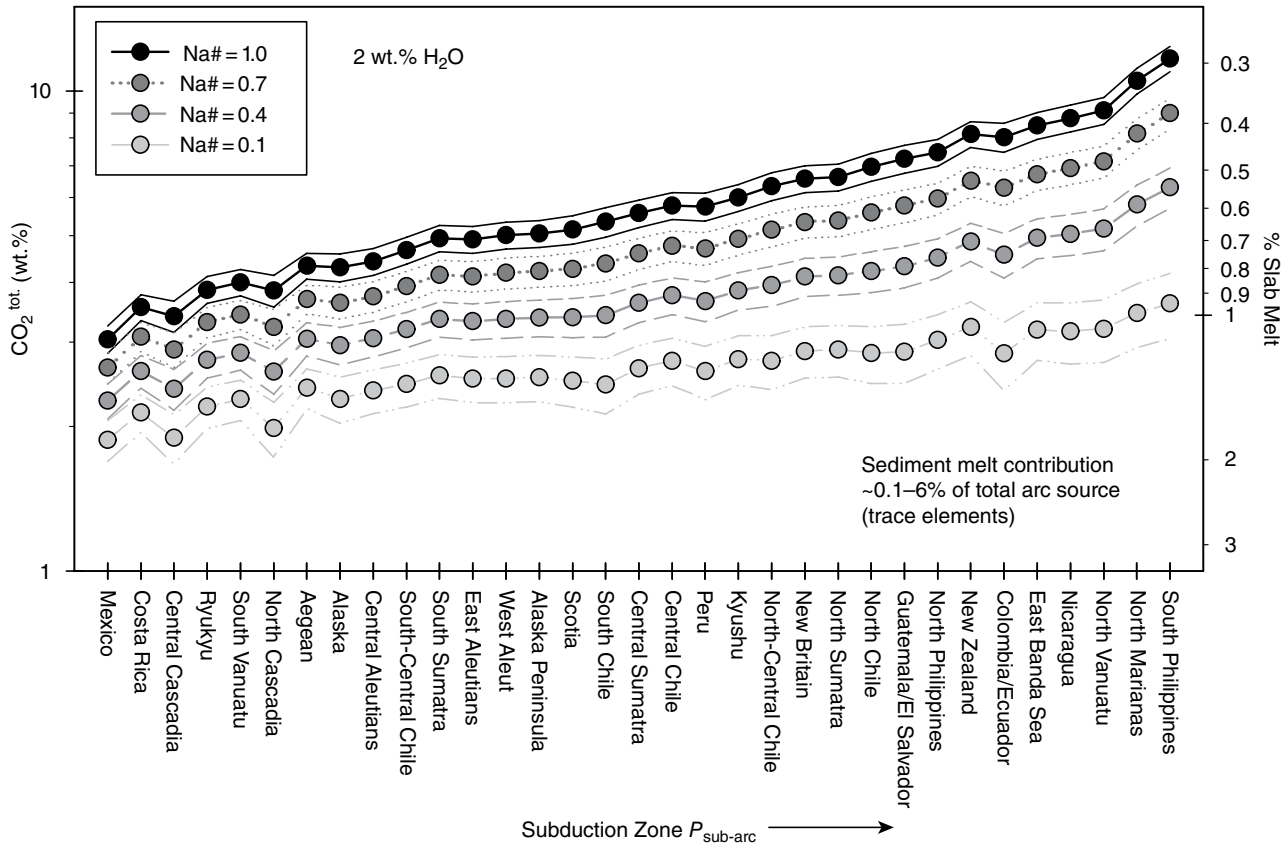

Figure 17.5 Total CO_2 content of rhyolitic slab melts (primary *y*-axis) calculated using the model for different melt Na# at fixed water content of 2 wt.% using calculated at the sub-arc *P-T* from the D80 model of Syracuse et al. (2010) for slabs above the hydrous solidus of Mann and Schmidt (2015). Subduction zones are arranged by increasing sub-arc depths. Calculated slab melt contribution to the sub-arc melt (secondary *y*-axis) assumes a primary arc basalt CO_2 content of 3000 ppm (Blundy et al., 2010; Wallace, 2005), an average mantle wedge CO_2 of 107 ppm (Cartigny et al., 2008; Dasgupta & Hirschmann, 2010; Hirschmann & Dasgupta, 2009), 15% mantle wedge melt, and mixing of mantle wedge-derived basaltic melt with a rhyolitic slab melt that is saturated in a CO_2-rich fluid (see Duncan & Dasgupta, 2015, for details). See electronic version for color representation of the figures in this book.

17.4.3. Implications for Slab-Mantle CO_2 Transfer in Subduction Zones

Our results indicate that changes in Na_2O versus K_2O concentrations in silicate melts have a significant effect on the CO_2 carrying capacities of slab-derived rhyolitic magmas at subduction zones. Because of this, variations in slab melt Na# and related variation in CO_2 carrying capacity can have significant impact on subduction zone carbon cycling efficiency. To illustrate this, we used our empirical fit to calculate the CO_2 content of slab melts and how much of such melts would be needed to mix with mantle melts to generate a primary arc basalt with 3000 ppm CO_2 (Blundy et al., 2010; Skora & Blundy, 2010; Wallace, 2005). If the extent of arc mantle source melting is 15%, the source mantle must contain 450 ppm CO_2, assuming batch melting and $D_C^{solid/melt}$ ~0. For example, based on the sub-arc conditions of North Cascadia, 3.09 GPa, 936 °C, from the D80 model of Syracuse et al. (2010), a slab melt with an Na# = 1 would have a saturated CO_2 content of 3.84 wt.%, assuming 2 wt.% H_2O is also present in the melt. For a given mantle wedge CO_2 content of 107 ppm (an average based on values from Cartigny et al., 2008; Dasgupta & Hirschmann, 2010; Hirschmann & Dasgupta, 2009; Marty, 2012; and Saal et al., 2002), the slab melt would only need to make up 0.89 wt.% of the total arc source region (Figure 17.5). We did this calculation for all slabs whose surface T at sub-arc depths fall above the hydrous solidus of Mann and Schmidt (2015).

According to this calculation, the CO_2-rich, fluid-saturated, rhyolitic slab melt contribution varies from 0.3% (Na# = 1.0) to 1.8% (Na# = 0.1), which is well within values of sediment contributions that are based on geochemistry of arc magmas (e.g., Class et al., 2000; Plank, 2005; Shimoda et al., 1998). Although we are extrapolating our empirical fit to a lower temperature range, the effect of temperature on CO_2 carrying capacity is small relative to the pressure effect (e.g., Duncan & Dasgupta, 2015) and the agreement with geochemical arguments from natural data gives us confidence that our values are reasonable as a point of discussion. Nevertheless, we emphasize that this model is intended to illustrate the importance of melt Na# on CO_2 transport from the slabs to the sub-arc mantle and is not intended to provide accurate estimates of slab melt contribution within individual arc segments.

In sub-arc settings with higher degrees of mantle wedge melting, lower water contents in the slab melts, CO_2-undersaturated silicic melt, and/or higher concentrations of CO_2 in primary arc magmas, a higher slab contribution to the sub-arc mantle would be required to generate estimated primary arc magma CO_2 concentrations. These effects have been observed and discussed in previous investigations of CO_2 cycling, but this calculation illustrates the additional importance of evaluating the impact of Na# in slab melts. According to our parametrization and calculations described here, differences in slab melt Na# could drive variations in slab contribution estimates by up to 120%.

17.5. CONCLUSIONS

We conducted high P-T experiments to determine the relationship between Na# and CO_2 in rhyolitic partial melts under pressure and temperatures relevant to subduction settings. Results indicate that there is likely a positive relationship between Na# of rhyolitic melts and carbonate dissolution, tied to changes in carbon speciation. The effect is stronger at higher pressures, where CO_3^{2-} dissolution in silicic melt becomes more significant. Our results could be interpreted to suggest greater affinity of CO_3^{2-} towards Na^+ rather than K^+, at least in silicic melts. No current CO_2 solubility models adequately capture the effect of melt Na/K ratio observed in our study. Future model regressions for CO_2 dissolution should be built differently, ensuring that effects of individual cation modifiers are reproduced. The melt compositional effect on CO_2 dissolution studied here has implications for carbon cycling in subduction settings. More specifically, our results indicate that accurately predicting carbon transport via slab melt in subduction zones requires taking the effects of network-modifying cation proportions on carbonate dissolution into consideration.

ACKNOWLEDGMENTS

We thank James Eguchi for his important discussion. Malcolm Massuyeau and an anonymous reviewer are acknowledged for their valuable comments on the original manuscript. The study was made possible by financial support from NSF grant OCE-1338842 and the Deep Carbon Observatory.

REFERENCES

Auzanneau, E., Vielzeuf, D., & Schmidt, M. W. (2006). Experimental evidence of decompression melting during exhumation of subducted continental crust. *Contrib. Mineral. Petrol.*, *152*(2), 125–148. doi:10.1007/s00410-006-0104-5

Blank, J. G., Stolper, E. M., & Carroll, M. R. (1993). Solubilities of carbon dioxide and water in rhyolitic melt at 850 °C and 750 bars. *Earth Planet. Sci. Lett.*, *119*(1–2), 27–36.

Blundy, J., Cashman, K. V., Rust, A., & Witham, F. (2010). A case for CO_2-rich arc magmas. *Earth Planet. Sci. Lett.*, *290*(3–4), 289–301. doi:10.1016/j.epsl.2009.12.013

Brey, G. (1976). CO_2 solubility and solubility mechanisms in silicate melts at high pressures. *Contrib. Mineral. Petrol.*, *57*(2), 215–221.

Brooker, R. A., Kohn, S. C., Holloway, J. R., & McMillan, P. F. (2001). Structural controls on the solubility of CO_2 in silicate melts: Part I. Bulk solubility data. *Chem. Geol.*, *174*(1–3), 225–239.

Carter, L. B., Skora, S., Blundy, J. D., De Hoog, J.C.M., & Elliott, T. (2015). An experimental study of trace element fluxes from subducted oceanic crust. *J. Petrol.*, *56*(8), 1585–1605. doi:10.1093/petrology/egv046

Cartigny, P., Pineau, F., Aubaud, C., & Javoy, M. (2008). Towards a consistent mantle carbon flux estimate: Insights from volatile systematics (H_2O/Ce, δD, CO_2/Nb) in the North Atlantic mantle (14°N and 34°N), *Earth Planet. Sci. Lett.*, *265*(3–4), 672–685. doi:10.1016/j.epsl.2007.11.011

Class, C., Miller, D. M., Goldstein, S. L., & Langmuir, C. H. (2000). Distinguishing melt and fluid subduction components in Umnak Volcanics, Aleutian Arc. *Geochem. Geophys. Geosys.*, *1*, 1004. doi:10.1029/1999gc000010

Cooper, L. B., Ruscitto, D. M., Plank, T., Wallace, P. J., Syracuse, E. M., & Manning, C. E. (2012). Global variations in H_2O/Ce: 1. Slab surface temperatures beneath volcanic arcs. *Geochem. Geophys. Geosys.*, *13*, Q03024. doi:10.1029/2011gc003902

Dasgupta, R. (2013). Ingassing, storage, and outgassing of terrestrial carbon through geologic time. *Rev. Mineral. Geochem.*, *75*, 183–229. doi:10.2138/rmg.2013.75.7

Dasgupta, R., & Hirschmann, M. M. (2010). The deep carbon cycle and melting in Earth's interior. *Earth Planet. Sci. Lett.*, *298*(1–2), 1–13. doi:10.1016/j.epsl.2010.06.039

de Leeuw, G.A.M., Hilton, D. R., Fischer, T. P., & Walker, J. A. (2007). The He-CO_2 isotope and relative abundance characteristics of geothermal fluids in El Salvador and Honduras: New constraints on volatile mass balance of the Central American Volcanic Arc. *Earth Planet. Sci. Lett.*, *258*(1–2), 132–146. doi:10.1016/j.epsl.2007.03.028

Dixon, J. E. (1997). Degassing of alkalic basalts. *Am. Mineral.*, *82*(3–4), 368–378.

Duncan, M. S., & Dasgupta, R. (2014). CO_2 solubility and speciation in rhyolitic sediment partial melts at 1.5–3.0 GPa: Implications for carbon flux in subduction zones. *Geochim. Cosmochim. Acta*, *124*, 328–347. doi:10.1016/j.gca.2013.09.026

Duncan, M. S., & Dasgupta, R. (2015). Pressure and temperature dependence of CO_2 solubility in hydrous rhyolitic melt: Implications for carbon transfer to mantle source of volcanic arcs via partial melt of subducting crustal lithologies. *Contrib. Mineral. Petrol.*, *169*(54). doi:10.1007/s00410-015-1144-5

Duncan, M. S., & Dasgupta, R. (2017). Rise of Earth's atmospheric oxygen controlled by efficient subduction of organic carbon. *Nat. Geosci.*, *10*(5), 387. doi:10.1038/Ngeo2939

Duncan, M. S., Dasgupta, R., & Tsuno, K. (2017). Experimental determination of CO_2 content at graphite saturation along a natural basalt-peridotite melt join: Implications for the fate of carbon in terrestrial magma oceans. *Earth Planet. Sci. Lett.*, *466*, 115–128. doi:10.1016/j.epsl.2017.03.008

Eguchi, J., & Dasgupta, R. (2018). A CO_2 solubility model for silicate melts from fluid saturation to graphite or diamond saturation. *Chem. Geol.*, *487*, 23–38. doi:10.1016/j.chemgeo.2018.04.012

Fogel, R. A., & Rutherford, M. J. (1990). The solubility of carbon dioxide in rhyolitic melts: A quantitative FTIR study. *Am. Mineral.*, *75*(11–12), 1311–1326.

Ghiorso, M. S., & Gualda, G.A.R. (2015). An H_2O-CO_2 mixed fluid saturation model compatible with rhyolite-MELTS. *Contrib. Mineral. Petrol.*, *169*(53). doi:10.1007/s00410-015-1141-8

Hayes, J. M., & Waldbauer, J. R. (2006). The carbon cycle and associated redox processes through time. *Philos. Trans. Roy. Soc. B*, *361*(1470). 931–950. doi:10.1098/rstb.2006.1840

Hermann, J., & Green, D. H. (2001). Experimental constraints on high pressure melting in subducted crust. *Earth Planet. Sci. Lett.*, *188*(1–2), 149–168.

Hermann, J., & Spandler, C. J. (2008). Sediment melts at sub-arc depths: An experimental study. *J. Petrol.*, *49*(4), 717–740. doi:10.1093/petrology/egm073.

Hirschmann, M. M., & Dasgupta, R. (2009). The H/C ratios of Earth's near-surface and deep reservoirs, and consequences for deep Earth volatile cycles. *Chem. Geol.*, *262*(1–2), 4–16. doi:10.1016/j.chemgeo.2009.02.008

Johnson, M. C., & Plank, T. (1999). Dehydration and melting experiments constrain the fate of subducted sediments. *Geochem. Geophys. Geosys.*, *1*, 1999GC000014.

Kelemen, P. B., & Manning, C. E. (2015). Reevaluating carbon fluxes in subduction zones, what goes down, mostly comes up. *Proc. Nat. Acad. Sci.*, *112*(30), E3997–E4006. doi:10.1073/pnas.1507889112

Kerrick, D. M., & Connolly, J.A.D. (2001). Metamorphic devolatilization of subducted oceanic metabasalts: Implications for seismicity, arc magmatism and volatile recycling. *Earth Planet. Sci. Lett.*, *189*(1–2), 19–29.

Klimm, K., Blundy, J. D., & Green, T. H. (2008). Trace element partitioning and accessory phase saturation during H_2O-saturated melting of basalt with implications for subduction zone chemical fluxes. *J. Petrol.*, *49*(3), 523–553. doi:10.1093/petrology/egn001

Konschak, A., & Keppler, H. (2014). The speciation of carbon dioxide in silicate melts. *Contrib. Mineral. Petrol.*, *167*(5), 998. doi:10.1007/S00410-014-0998-2

Lange, R. A., & Carmichael, I.S.E. (1987). Densities of Na_2O-K_2O-CaO-MgO-FeO-Fe_2O_3-Al_2O_3-TiO_2-SiO_2 liquids: New measurements and derived partial molar properties. *Geochim. Cosmochim. Acta*, *51*(11), 2931–2946.

Laurie, A., & Stevens, G. (2012). Water-present eclogite melting to produce Earth's early felsic crust. *Chem. Geol.*, *314*, 83–95. doi:10.1016/j.chemgeo.2012.05.001

Mann, U., & Schmidt, M. W. (2015). Melting of pelitic sediments at subarc depths: 1. Flux vs. fluid-absent melting and a parameterization of melt productivity. *Chem. Geol.*, *404*, 150–167. doi:10.1016/j.chemgeo.2015.02.032

Martin, L.A.J., & Hermann, J. (2018). Experimental phase relations in altered oceanic crust: Implications for carbon recycling at subduction zones. *J. Petrol.*, *59*(2), 299–320. doi:10.1093/petrology/egy031

Marty, B. (2012). The origins and concentrations of water, carbon, nitrogen and noble gases on Earth. *Earth Planet. Sci. Lett.*, *313*, 56–66. doi:10.1016/j.epsl.2011.10.040

Morizet, Y., Kohn, S. C., & Brooker, R. A. (2001). Annealing experiments on CO_2-bearing jadeite glass: An insight into the true temperature dependence of CO_2 speciation in silicate melts. *Mineral. Mag.*, *65*(6), 701–707.

Morizet, Y., Paris, M., Gaillard, F., & Scaillet, B. (2014). Carbon dioxide in silica-undersaturated melt: Part I. The effect of mixed

alkalis (K and Na) on CO_2 solubility and speciation. *Geochim. Cosmochim. Acta*, *141*, 45–61. doi:10.1016/j.gca.2014.06.014

Mysen, B. O. (1976). Role of volatiles in silicate melts: Solubility of carbon dioxide and water in feldspar, pyroxene, and feldpathoid melts to 30 kb and 1625 °C. *Am. J. Sci.*, *276*(8), 969–996.

Mysen, B. O., Eggler, D. H., Seitz, M. G., & Holloway, J. R. (1976). Carbon dioxide in silicate melts and crystals: 1. Solubility measurements. *Am. J. Sci.*, *276*(4), 455–479.

Mysen, B. O., & Virgo, D. (1980a). The solubility behavior of CO_2 in melts on the join $NaAlSi_3O_8$-$CaAl_2Si_2O_8$-CO_2 at high pressures and temperatures: A Raman spectroscopic study. *Am. Mineral.*, *65*, 1166–1175.

Mysen, B. O., & Virgo, D. (1980b). Solubility mechanisms of carbon dioxide in silicate metals: A Raman spectroscopic study. *Am. Mineral.*, *65*(9–10), 885–899.

Newman, S., Stolper, E. M., & Epstein, S. (1986). Measurement of water in rhyolitic glasses: Calibration of an infrared spectroscopic technique. *Am. Mineral.*, *71*(11–12), 1527–1541.

Ni, H. W., & Keppler, H. (2013). Carbon in silicate melts. *Rev. Mineral. Geochem.*, *75*, 251–287. doi:10.2138/rmg.2013.75.9

Nowak, M., Porbatzki, D., Spickenbom, K., & Diedrich, O. (2003). Carbon dioxide speciation in silicate melts: A restart. *Earth Planet. Sci. Lett.*, *207*(1–4), 131–139. doi:10.1016/S0012-821x(02)01145-7

Plank, T. (2005). Constraints from thorium/lanthanum on sediment recycling at subduction zones and the evolution of the continents. *J. Petrol.*, *46*(5), 921–944. doi:10.1093/petrology/egi005

Poli, S., & Schmidt, M. W. (2002). Petrology of subducted slabs. *Ann. Rev. Earth Planet. Sci.*, *30*, 207–235.

Prouteau, G., Scaillet, B., Pichavant, M., & Maury, R. (2001). Evidence for mantle metasomatism by hydrous silicic melts derived from subducted oceanic crust. *Nature*, *410*(6825), 197–200.

Qian, Q., & Hermann, J. (2013). Partial melting of lower crust at 10–15 kbar: Constraints on adakite and TTG formation. *Contrib. Mineral. Petrol.*, *165*(6), 1195–1224. doi:10.1007/s00410-013-0854-9

Rapp, R. P., & Watson, E. B. (1995). Dehydration melting of metabasalt at 8–32 kbar: Implications for continental growth and crust-mantle recycling. *J. Petrol.*, *36*(4), 891–931.

Saal, A. E., Hauri, E. H., Langmuir, C. H., & Perfit, M. R. (2002). Vapour undersaturation in primitive mid-ocean-ridge basalt and the volatile content of Earth's upper mantle. *Nature*, *419*(6906), 451–455. doi:10.1038/Nature01073

Sano, Y., & Williams, S. N. (1996). Fluxes of mantle and subducted carbon along convergent plate boundaries. *Geophys. Res. Lett.*, *23*(20), 2749–2752.

Schmidt, M. W. (2015). Melting of pelitic sediments at subarc depths: 2. Melt chemistry, viscosities and a parameterization of melt composition. *Chem. Geol.*, *404*, 168–182. doi:10.1016/j.chemgeo.2015.02.013

Schmidt, M. W., Vielzeuf, D., & Auzanneau, E. (2004). Melting and dissolution of subducting crust at high pressures: The key role of white mica. *Earth Planet. Sci. Lett.*, *228*(1–2), 65–84. doi:10.1016/j.epsl.2004.09.020

Sen, C., & Dunn, T. (1994). Dehydration melting of a basaltic composition amphibolite at 1.5 and 2.0 GPa: Implications for the origin of adakites. *Contrib. Mineral. Petrol.*, *117*(4), 394–409. doi:10.1007/Bf00307273

Shaw, A. M., Hilton, D. R., Fischer, T. P., Walker, J. A., & Alvarado, G. E. (2003). Contrasting He-C relationships in Nicaragua and Costa Rica: Insights into C cycling through subduction zones. *Earth Planet. Sci. Lett.*, *214*(3–4), 499–513. doi:10.1016/S0012-821x(03)00401-1

Shimoda, G., Tatsumi, Y., Nohda, S., Ishizaka, K., & Jahn, B. M. (1998). Setouchi high-Mg andesites revisited: Geochemical evidence for melting of subducting sediments. *Earth Planet. Sci. Lett.*, *160*(3–4), 479–492.

Silver, L., & Stolper, E. (1989). Water in albitic glasses. *J. Petrol.*, *30*(3), 667–709.

Silver, L. A. (1988). Water in silicate glasses (Ph. D. thesis). California Institute of Technology, Pasadena, CA.

Skora, S., & Blundy, J. (2010). High-pressure hydrous phase relations of radiolarian clay and implications for the involvement of subducted sediment in arc magmatism. *J. Petrol.*, *51*(11), 2211–2243. doi:10.1093/petrology/egq054

Skora, S., Blundy, J. D., Brooker, R. A., Green, E.C.R., de Hoog, J.C.M., & Connolly, J.A.D. (2015). Hydrous phase relations and trace element partitioning behaviour in calcareous sediments at subduction zone conditions. *J. Petrol.*, *56*(5), 953–980. doi:10.1093/petrology/egv024

Sleep, N. H., & Zahnle, K. (2001). Carbon dioxide cycling and implications for climate on ancient Earth. *J. Geophys. Res.*, *106*(E1), 1373–1399.

Spandler, C., Yaxley, G., Green, D. H., & Scott, D. (2010). Experimental phase and melting relations of metapelite in the upper mantle: Implications for the petrogenesis of intraplate magmas. *Contrib. Mineral. Petrol.*, *160*(4), 569–589. doi:10.1007/s00410-010-0494-2

Stolper, E., Fine, G., Johnson, T., & Newman, S. (1987). Solubility of carbon dioxide in albitic melt. *Am. Mineral.*, *72*(11–12), 1071–1085.

Syracuse, E. M., van Keken, P. E., & Abers, G. A. (2010). The global range of subduction zone thermal models. *Phys. Earth Planet. Inter.*, *183*(1–2), 73–90. doi:10.1016/j.pepi.2010.02.004

Tamic, N., Behrens, H., & Holtz, F. (2001). The solubility of H_2O and CO_2 in rhyolitic melts in equilibrium with a mixed CO_2-H_2O fluid phase. *Chem. Geol.*, *174*(1–3), 333–347.

Thomsen, T. B., & Schmidt, M. W. (2008). Melting of carbonated pelites at 2.5–5.0 GPa, silicate-carbonatite liquid immiscibility, and potassium-carbon metasomatism of the mantle. *Earth Planet. Sci. Lett.*, *267*(1–2), 17–31. doi:10.1016/j.epsl.2007.11.027

Thomson, A. R., Walter, M. J., Kohn, S. C., & Brooker, R. A. (2016). Slab melting as a barrier to deep carbon subduction. *Nature*, *529*(7584), 76. doi:10.1038/nature16174

Tsuno, K., & Dasgupta, R. (2011). Melting phase relation of nominally anhydrous, carbonated pelitic-eclogite at 2.5–3.0 GPa and deep cycling of sedimentary carbon. *Contrib. Mineral. Petrol.*, *161*, 743–763. doi:10.1007/s00410-010-0560-9

Tsuno, K., & Dasgupta, R. (2012). The effect of carbonates on near-solidus melting of pelite at 3 GPa: Relative efficiency of H_2O and CO_2 subduction. *Earth Planet. Sci. Lett.*, *319*, 185–196. doi:10.1016/j.epsl.2011.12.007

Tsuno, K., Dasgupta, R., Danielson, L., & Righter, K. (2012). Flux of carbonate melt from deeply subducted pelitic sediments: Geophysical and geochemical implications for the source of Central American volcanic arc. *Geophys. Res. Lett.*, *39*, L16307. doi:10.1029/2012gl052606

Vetere, F., Holtz, F., Behrens, H., Botcharnikov, R. E., & Fanara, S. (2014). The effect of alkalis and polymerization on the solubility of H_2O and CO_2 in alkali-rich silicate melts. *Contrib. Mineral. Petrol.*, *167*(5). doi:10.1007/S00410-014-1014-6

Wallace, P. J. (2005). Volatiles in subduction zone magmas: Concentrations and fluxes based on melt inclusion and volcanic gas data. *J. Volcanol. Geotherm. Res.*, *140*(1–3), 217–240. doi:10.1016/j.jvolgeores.2004.07.023

Wolff, P. E., Koepke, J., & Feig, S. T. (2013). The reaction mechanism of fluid-induced partial melting of gabbro in the oceanic crust. *Eur. J. Mineral.*, *25*(3), 279–298. doi:10.1127/0935-1221/2013/0025-2314

Zhang, Y. X., Stolper, E. M., & Ihinger, P. D. (1995). Kinetics of the reaction $H_2O + O = 2OH$ in rhyolitic and albitic glasses: Preliminary results. *Am. Mineral.*, *80*(5–6), 593–612.